Green Chemistry

PAPER

Check for updates

Lignification-mimetic dehydrogenative diphenoquinone synthesis and electrochemical CO_2 capture

Hyeyun Kim,[a] Omer Shinnawy,[b] Seda Ulusoy,[c] Germán Salazar-Alvarez, [d]
Ngoc Tuan Tran,[e] Hyesung Cho,[a] Changmin Sung, [f] Seung-Soo Kim, [g]
Bonwook Koo, [h] Keunhong Jeong,[i] Kiana Amini[b] and Kwang Ho Kim *[e]

Sustainable mitigation of atmospheric CO_2 requires not only efficient capture technologies but also environmentally responsible production of the materials that enable them. Many capture systems rely on materials synthesized *via* energy-intensive, multi-step processes from non-renewable feedstocks. To create truly sustainable solutions, there is a critical need for green synthetic pathways that minimize the overall carbon footprint of capture technologies from cradle to grave. Here, we report a diphenoquinone-based CO_2 capture material synthesized from the lignin-derived monomer *via* an enzymatic coupling reaction, establishing a sustainable route under mild, aqueous conditions without complex purification. The reaction selectively forms a crystalline C4–C4' linked diphenoquinone, confirmed by comprehensive spectroscopic analyses, and avoids the structural heterogeneity typical of lignin-derived products. The resulting molecule exhibits a positive redox potential and robust reversibility, enabling electrochemical CO_2 capture and release with a specific capacity of 1.9 mmol g^{-1}. While initial performance is limited by the physical stability of the reduced species, this work establishes a new paradigm for lignin valorization by transforming renewable phenolics into discrete, functional molecules for CO_2 capture, and offers a broadly applicable platform for green synthesis of bio-derived quinones, providing a foundation for sustainable technologies within a circular carbon economy.

Green foundation

1. This work advances green chemistry by introducing a biomimetic, lignification-inspired synthesis that transforms a renewable lignin monomer into a discrete, redox-active diphenoquinone under mild, aqueous conditions. It establishes a sustainable link between biomass valorization and electrochemical CO_2 capture.

2. The method replaces fossil-based reagents and multi-step, high-energy syntheses with a one-pot, enzymatic route carried out at room temperature in water, eliminating toxic solvents and minimizing chemical waste while maintaining functional performance.

3. The work could be made greener and elevated by incorporating enzyme immobilization and reuse, solvent recycling, and renewable electricity for electrochemical operation. Further research will focus on improving the stability of reduced species, conducting life-cycle assessments to quantify overall sustainability benefits.

[a]Extreme Materials Research Center, Korea Institute of Science and Technology,
5 Hwarang-ro 14-gil, Seongbuk-gu, Seoul, 02792, Republic of Korea
[b]Department of Materials Engineering, University of British Columbia, 6350 Stores
Road, Vancouver, BC V6T 1Z4, Canada
[c]Heinz Maier-Leibnitz Zentrum (MLZ), Technische Universität München,
Lichtenbergstr. 1, 85748 Garching, Germany
[d]Department of Materials Science and Engineering, Uppsala University,
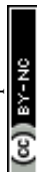75103 Uppsala, Sweden

[e]Department of Wood Science, Faculty of Forestry, University of British Columbia,
2424 Main Mall, Vancouver, BC V6T 1Z4, Canada. E-mail: kwang.kim@ubc.ca
[f]Doping Control Center, Korea Institute of Science and Technology, 5 Hwarang-ro
14-gil, Seongbuk-gu, Seoul, Korea
[g]Department of Chemical Engineering, Kangwon National University, 346 Joongang-
ro, Samcheok, Gangwon-do 25913, South Korea
[h]School of Forestry Sciences and Landscape Architecture, Kyungpook National
University, Daegu 41566, Republic of Korea
[i]Department of Chemistry, Korea Military Academy, Seoul 01805, Republic of Korea

Introduction

Anthropogenic carbon dioxide (CO_2) emissions are a primary driver of the global climate crisis, posing substantial risks to ecosystems and human health. Despite significant efforts to transition from fossil fuels to renewable energy sources such as biofuels and electricity, certain sectors remain difficult to decarbonize. Given the urgency of mitigating greenhouse gas emissions, the development of carbon removal technologies, whether through point-source capture or direct air capture, is essential. Advancing these technologies through rapid development, scaling up, and implementation is critical to achieving a net-zero emission economy.[1]

Conventional carbon capture and sequestration (CCS) technologies have primarily focused on capturing CO_2 from large-scale emitters and storing it in secure geologic reservoirs.[2,3] Among these, amine-based thermal scrubbing is one of the most widely used methods. This process captures CO_2 through chemisorption and releases it *via* a temperature-swing regeneration cycle. While effective, this approach has notable drawbacks, including high energy consumption during regeneration, chemical degradation of the sorbents, and relatively slow CO_2 adsorption kinetics.[4-7] To overcome these limitations, electrochemically mediated carbon capture has emerged as a promising alternative. This strategy offers several advantages: it operates under ambient temperature and pressure conditions, produces no harmful byproducts, and can be tailored using a wide range of candidate molecules, making electrochemical carbon capture a more sustainable and flexible pathway towards scalable CO_2 mitigation.[8]

While various classes of organic molecules, including N-heterocycles and organometallic complexes, have been investigated, quinone-based systems have emerged as leading candidates due to their inherent structural stability, tunable redox properties, and efficient nucleophilic CO_2 capture mechanism.[9] Widely found in nature, quinones function as redox-active electron-transfer agents in fundamental biological processes such as respiration and photosynthesis. Featuring structural diversity and tunability, the ability of typical quinones to undergo rapid and reversible reductions makes them attractive candidates for use in energy storage systems (*i.e.*, aqueous flow battery system).[10-12] The electrochemically reduced forms of quinones (*i.e.*, oxyanion nucleophiles) show a high binding affinity to CO_2,[13] enabling effective separation and concentration of CO_2 from various sources. Their reversible redox behavior and structural versatility position them as effective organic compounds for sustainable CO_2 capture systems.[13-19]

Quinone-based systems enable CO_2 capture and release through two distinct mechanisms: the nucleophilicity-swing and the pH-swing.[20] The nucleophilicity-swing mechanism operates in aprotic or protic solvents containing dissolved quinones as well as in quinone-immobilized electrodes. In this mechanism, reduced quinones (phenolate forms) react reversibly with CO_2 through nucleophilic addition, leading to the formation of quinone-CO_2 adducts. In contrast, the pH-swing mechanism involves quinones in protic solvents, where, depending on the pK_a of the quinone, the electrochemical reduction of quinones can be proton-coupled and create hydroxide ions, capturing CO_2 as carbonate or bicarbonate.

Among quinonoid structures, diphenoquinones constitute a unique subclass in which the carbonyl groups are located on separate aromatic rings, allowing extended conjugation. Whereas the two-electron reduction of benzoquinone produces a dianion with a single aromatic ring, diphenoquinone yields a dianion with two aromatic rings and enhanced charge delocalization. This increased delocalization contributes to the generally more positive redox potentials observed for diphenoquinones relative to their benzoquinone analogues.[21] Additionally, the rigid and extended planar structure of diphenoquinones imparts high structural stability and reduced solubility, making them inherently more suitable than simple benzoquinones for electrode applications in liquid electrolyte systems.[21]

While quinones are highly desirable for functional applications and are abundant in nature, their industrial-scale supply is dominated by chemical synthesis from petroleum-based sources. This reliance presents a sustainability conflict, as conventional methods often involve multi-step routes with harsh chemicals and significant energy consumption.[21,22] To address these limitations, a new design strategy for CO_2 capture materials is required, considering the entire lifecycle, from a renewable resource to a synthesis process with a minimal environmental footprint.

Lignin is a vast source of quinones, as the Earth's most abundant aromatic biopolymer and a massive byproduct of the pulp industry.[23,24] This has naturally led to its exploration for CO_2 capture but its quinone-like structures viable for electrochemical carbon adsorption was neglected. For example, previous studies of utilization of lignin-derived materials for CO_2 capture has predominantly involved high-temperature pyrolysis to produce porous carbons for thermal physisorption, a process that destroys lignin's inherent chemical functionality, using it as merely a passive carbon supporter.[25-27] While these materials can exhibit high capacities (0.4–11 mmol CO_2 per g), this performance comes at a significant cost requiring further energy input for thermal regeneration. More recently, Ghorai *et al.* demonstrated the chemical modification of the lignin polymer with ionic groups for thermal chemisorption, preserving the polymer backbone and enabling regeneration with mild heat with good cyclability and moderate capacity.[28,29] Although lignin-based materials have been successfully demonstrated as renewable carbon backbones, leveraging the intrinsic redox functionality of lignin-derived quinone motifs represents a significant advance toward their high-value valorization for sustainable CO_2 capture.

In this work, we demonstrated a sustainable synthesis of a lignin-derived quinone based redox-active electrochemical CO_2 capture material. This was achieved *via* a biomimetic, peroxidase-catalyzed radical polymerization of syringol (2,6-dimethoxyphenol) inspired by *in vitro* lignification. The resulting dehydrogenation compound, a syringol-derived dipheno-

quinone, (3,3′,5,5′-tetramethoxy-4,4′-diphenoquinone) was comprehensively characterized and subsequently utilized as a redox-active material for electrochemical CO_2 capture. The enzymatic synthesis itself adheres to the core principles of green chemistry, proceeding under mild aqueous conditions without external heating or pressurization. However, while methods mimicking lignification are prevalent for synthesizing structural biopolymers, their potential to generate functional, redox-active materials for electrochemical applications has been largely overlooked. To the best of our knowledge, this work represents the first demonstration of electrochemical CO_2 capture using a material synthesized *via* bio-catalysis from a lignin-derived precursor. This nature-inspired strategy addresses a challenge of state-of-the-art electrochemically redox-active materials for this purpose by establishing a complete 'green' value chain: from a renewable resource and a mild, biomimetic synthesis to a final, critical environmental application. This work not only revitalizes a classical enzymatic synthesis pathway but also offer a sustainable route to quinonoid materials, bypassing the severe processing typical of lignin valorization.

Results

Biomimetic synthesis of diphenoquinone

Lignin-like dehydrogenation polymers (DHPs) and their synthesis have been extensively studied to elucidate the structure of lignin and understand the process of natural lignification in plant cell walls.[30,31] In nature, lignin is an enzyme-initiated biopolymer formed through random radical coupling reactions of at least two monolignol precursors (*e.g.*, *p*-coumaryl alcohol, coniferyl alcohol, and sinapyl alcohol).[32] Upon oxidation by peroxidase, these precursors generate delocalized radicals with unpaired electron density at the 1-, 3-, O-4-, 5-, and β-positions (Fig. S1). Previous studies have reported high spin density at the O4 position,[33,34] suggesting it as the most reactive site for radical coupling. Additionally, the $C_β$ position is favored due to reduced steric hindrance from methoxyl groups. These features contribute to the high abundance of β-O-4 linkages in the native lignin structure. Beyond the radical coupling by three representative monolignols, lignin polymerization is known for its plasticity, allowing the incorporation of various phenolic compounds that reach lignification sites in the plant cell wall.[35]

The outcome of peroxidase-catalyzed oxidation depends on the precursor. Phenolic precursors (*e.g.*, syringol and guaiacol), which lack an aliphatic side chain, form phenoxy radical that promotes selective C4–C4′ coupling, yielding stable diphenol dimers.[36–38] Understanding this highly selective pathway provides a biomimetic strategy for the precise synthesis of functional diphenols and diphenoquinones, avoiding the structural complexity of traditional lignin polymerization.

Inspired by this natural polymerization mechanism, we selectively produce a diphenoquinone structure *via* radical coupling at a specific position while suppressing undesired linkages. Syringol (2,6-dimethoxyphenol) has symmetric substitution pattern with two methoxy groups at C2 and C6 impose significant steric hindrance at the *ortho* positions, effectively blocking those sites from participating in coupling reactions. This steric constraint makes the *para* position (C4) the most accessible and reactive site. Consequently, syringol favors symmetrical C4–C4′ coupling, leading to the formation of a well-defined diphenoquinone structure, in contrast to the diverse linkage patterns typically observed in lignification with coniferyl alcohol or sinapyl alcohol.

Fig. 1 illustrates the mesomeric structures of the syringol phenoxy radical, spin density contour plots, and the calculated
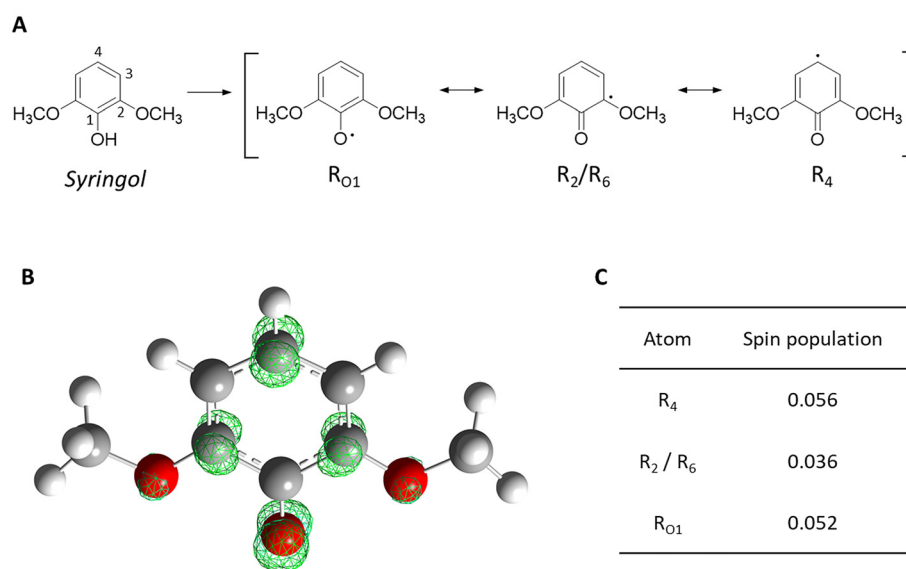

Fig. 1 (A) Primary mesomeric forms of a phenoxy radical produced by dehydrogenative reaction of syringol, (B) spin density contour plots, and (C) calculated spin populations for syringol radicals, obtained using the M06-2X meta-hybrid functional and the 6-31+G(2d,2p) basis set.

Atom	Spin population
R_4	0.056
R_2 / R_6	0.036
R_{O1}	0.052

spin populations at each reactive site. As shown, the unpaired electron is predominantly localized at the C4 position. It is noted that C4 in syringol corresponds to the C1 position in conventional monolignols, where the aliphatic side chain is typically located. This localization suggests that radical coupling preferentially occurs at C4, facilitating radical termination and the formation of a diphenoquinone structure. In contrast, the steric hindrance from methoxy groups at C2 and C6 likely suppresses alternative coupling pathways. Interestingly, the O1 site also exhibited relatively high spin density, suggesting its potential as an alternative reactive site. This finding raises the possibility that 1-O-linked chain-propagation products could form under certain conditions.

To validate this hypothesis, peroxidase-catalyzed dehydrogenation of syringol was conducted *in vitro* using a continuous addition mode to enable controlled radical coupling reaction. The resulting deep purple-colored solid was isolated and subjected to comprehensive characterization. LC-MS/MS analysis confirmed the formation of a syringol-derived diphenoquinone, with a distinct signal at *m/z* 305.26 ([M + H]$^+$), corresponding to 3,3′,5,5′-tetramethoxy-4,4′-diphenoquinone (Fig. S2 and Fig. 2A). Further analysis by gel permeation chromatography (GPC) revealed a single sharp peak between 300 and 400 Da (Fig. 2B). Unlike conventional DHPs derived from lignin monolignols, which typically exhibit molecular weights greater than 3000 g mol^{-1},[39–42] the syringol-derived product displayed a significantly lower average molecular weight (M_w = 350 g mol^{-1}) and an exceptionally narrow polydispersity index (PDI = 1.03). These results strongly support of a discrete dimeric structure, consistent with the expected diphenoquinone.

In addition to the diphenoquinone form, a hydroquinone form, 4,4′-dihydroxy-3,3′,5,5′-tetramethoxybiphenyl, was also detected by LC-MS analysis at *m/z* of 307.28 (Fig. S2). Although the signal intensity was relatively low, the presence of this hydroquinone form was confirmed. The formation of hydroquinone may be attributed to self-disproportionation of diphenoquinone, leading to production of semiquinone and hydroquinone species.[43,44] Additionally, under the oxidative conditions employed (peroxidase + H$_2$O$_2$), the oxidized peroxidase can produce semiquinone radicals, which may engage in radical redox cycling, ultimately reducing diphenoquinone to its hydroquinone counterpart. Thus, the reaction mixture predominantly yielded a deep purple solid, characteristic of the quinhydrone pillars by charge-transfer complex forming a co-crystal of quinone and hydroquinone (see Fig. S3 for an image of the synthesized product). Dissolution of the quinhydrone crystals disrupts the intermolecular non-covalent forces (charge-transfer, π-stacking, and hydrogen bonding) holding the complex together, causing it to dissociate into its constituent quinone and hydroquinone molecules. The unstable hydroquinone is then readily oxidized by atmospheric oxygen during solvent evaporation. As a result, the final extract obtained for analysis is composed dominantly of the more stable diphenoquinone.[45]

The structure of the synthesized compound was confirmed by FT-IR and ^{1}H NMR spectroscopy as shown in Fig. 3A and B. The measured FT-IR spectrum is consistent with the reference spectrum reported in the NIST Chemistry WebBook for 3,3′,5,5′-tetramethoxy-4,4′-diphenoquinone, supporting the assigned functional-group vibrational bands.[46] The presence of the aromatic rings was confirmed by C═C stretching vibrations observed between 1440–1660 cm^{-1} (a) and out-of-plane C–H bending at 710–920 cm^{-1} (b). Key stretches for the methoxy substituents were identified, including the C–H bending of the methyl groups at 1200–1437 cm^{-1} (c) and symmetric C–O stretch at 1110 cm^{-1} (d). A strong absorption band centered at 1624 cm^{-1}, accompanied by a shoulder near 1610 cm^{-1}, is assigned to the conjugated quinone C═O stretching mode, partially overlapping with aromatic C═C vibrations within the 1440–1660 cm^{-1} region. A weak absorption near 3300 cm^{-1}, corresponding to an O–H stretch, indicated a minor amount of free OH groups due to highly ordered hydrogen bonding between OH from hydroquinone and carbonyl oxygen of the neighboring diphenoquinone.

The ^{1}H NMR spectrum provided further definitive evidence. The signal at δ 3.8 ppm corresponds to the twelve protons of the four equivalent methoxy groups (c in Fig. 3A), while the signal at δ 6.8 ppm is assigned to the four equivalent aromatic protons (b). These combined data are fully consistent with the
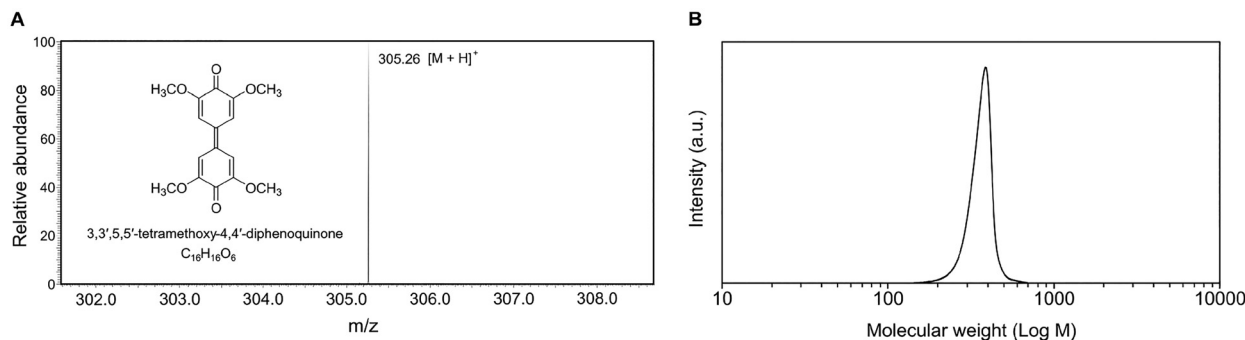

Fig. 2 (A) Mass spectrum of 3,3′,5,5′-tetramethoxy-4,4′-diphenoquinone (*m/z* 305.26) observed from the analysis of syringol-derived dehydrogenation compound by LC-MS/MS and (B) gel permeation chromatogram, showing a clear peak between 300 and 400 Da.
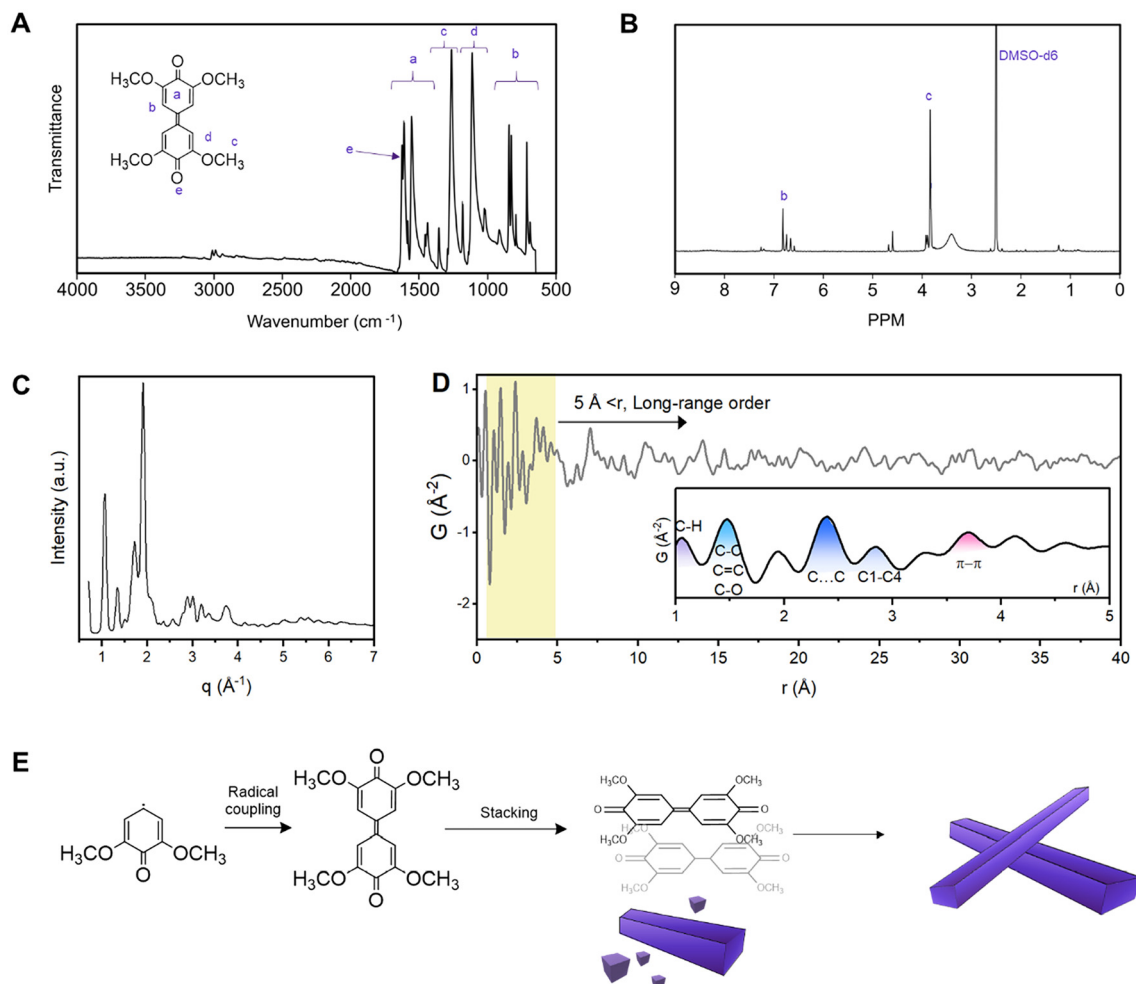
Fig. 3 (A) Fourier-transform infrared (FT-IR) spectrum, (B) ^{1}H nuclear magnetic resonance (NMR) spectrum, and (C) X-ray diffraction, (D) atomic PDF analysis of the synthesized dehydrogenative compound, (E) scheme of molecular structure changes of syringol diphenoquinone.

structure of 3,3′,5,5′-tetramethoxy-4,4′-diphenoquinone. Minor peaks at 3.5 and 6.8 ppm are attributed to trace impurities introduced during the biomimetic enzymatic synthesis (*e.g.*, protein residues or a small amount of the corresponding hydroquinone analogue), consistent with the previous studies using same method but laccase,[47] as well as residual water at 4.7 ppm; however, LC/MS confirms diphenoquinone as the dominant product, and these minor signals do not affect the structural assignment.

The structure of the product from the syringol dehydrogenation reaction was investigated using wide-angle X-ray scattering (WAXS) and pair distribution function (PDF) analysis. Contrary to the "polymer" designation, the WAXS pattern revealed sharp Bragg peaks, characteristic of a highly crystalline material. This finding is consistent with the visual observation of fiber-like crystals precipitating from the reaction medium and literature.[21]

PDF analysis corroborated crystalline structure that persist to high *r* (>30 Å), a clear signature of long-range periodic order (Fig. 3D). The low-*r* region (<4 Å) is dominated by sharp intramolecular peaks consistent with a rigid diphenoquinone-like molecule. Distinct peaks observed at 1.395, 2.416, and 2.79 Å correspond to the expected carbon–carbon and carbon–oxygen bond distances within and between aromatic rings (Table S1).[48,49] An intermolecular peak at *r* ≈ 3.7 Å indicates that the planar, short-length molecules readily self-assemble into highly ordered columnar structures, driven by strong intermolecular interactions rather than covalent chain connections. If the radical were predominantly delocalized at the phenolic oxygen, one would expect the formation of 1-O-4 linked oligomers or polymers. However, the absence of signal in the 4.8–5.2 Å range (distance known for 1-O-4 linked dimers) further supports our hypothesis that 4–4 coupling is the dominant pathway under the conditions tested.[50,51]

These combined results indicate that the peroxidase-catalyzed radical coupling of syringol selectively produce a dimer, identified as 3,3′,5,5′-tetramethoxy-4,4′-diphenoquinone. Then Fig. 3E depicts radical coupling producing syringol-derived

diphenoquinone that this well-defined, short-length molecule then readily self-assembles *via* π–π stacking to form the observed highly ordered, crystalline structures.

Scanning electron microscopy (SEM) revealed that the syringol-derived diphenoquinone crystallized into well-defined prism-like microstructures under the typical synthesis conditions, which involved gentle stirring at 200 rpm (Fig. 4A). These columnar crystals exhibited uniform dimensions with smooth surface and sharp, angular facets, indicative of highly ordered growth. A higher-magnification image further highlights the regular geometry and compact arrangement of the crystals. A previous report on crystallographic data of 3,3′,5,5′-tetramethoxy-4,4′-diphenoquinone revealed that this diphenoquinone belongs to the monoclinic space group, which is exactly observed from the SEM images here.

To explore potential control over crystal morphology, we investigated the effect of synthesis parameter, including stirring conditions. When the reaction was carried out without stirring, the resulting product displayed a markedly different morphology, forming long and highly entangled structures (Fig. 4B). These needle-like one dimensional formation suggest unregulated and anisotropic crystal growth in the absence of mixing. This morphological shift demonstrates the size-controllable synthesis of diphenoquinone, where simple changes to the reaction environment can modulate the crystal dimensions and aspect ratio. The ability to tune the size and shape of the resulting microstructures not only provides

insight into the kinetics of radical-mediated crystallization, but also opens opportunities to tailor material properties for specific applications.

To further investigate the crystallization behavior, we employed a high-speed camera to monitor the formation of the syringol-derived dehydrogenative compound in real time. Remarkably, crystal growth initiated immediately upon addition of the precursor, and the entire reaction was completed within several minutes, as clearly captured in the video (SI Video S1). This rapid formation emphasizes the efficiency of the peroxidase-catalyzed process, which contrasts largely with conventional chemical synthesis routes for diphenoquinone that typically require ~20 h, involve multiple steps, and utilize numerous chemical reagents. In comparison, our method offers a greener and more sustainable alternative, minimizing time, reagents, and energy input. The *in situ* optical microscopy image shown in Fig. 4C was taken 5 min after precursor addition, capturing the rapid emergence of elongated, thread-like crystals. These observations, together with SEM analysis, demonstrate the feasibility of using biocatalytic radical coupling to synthesize structurally ordered diphenoquinones in a fast, low-environmental impact manner.

Thermogravimetric analysis (TGA) of the crystalline product (Fig. S4) reveals excellent thermal stability, with a decomposition temperature exceeding 300 °C unlike amorphous lignin polymers with a low glass transition temperature ($T_g \approx 150$ °C). Such superior thermal resistivity is a direct consequence of the
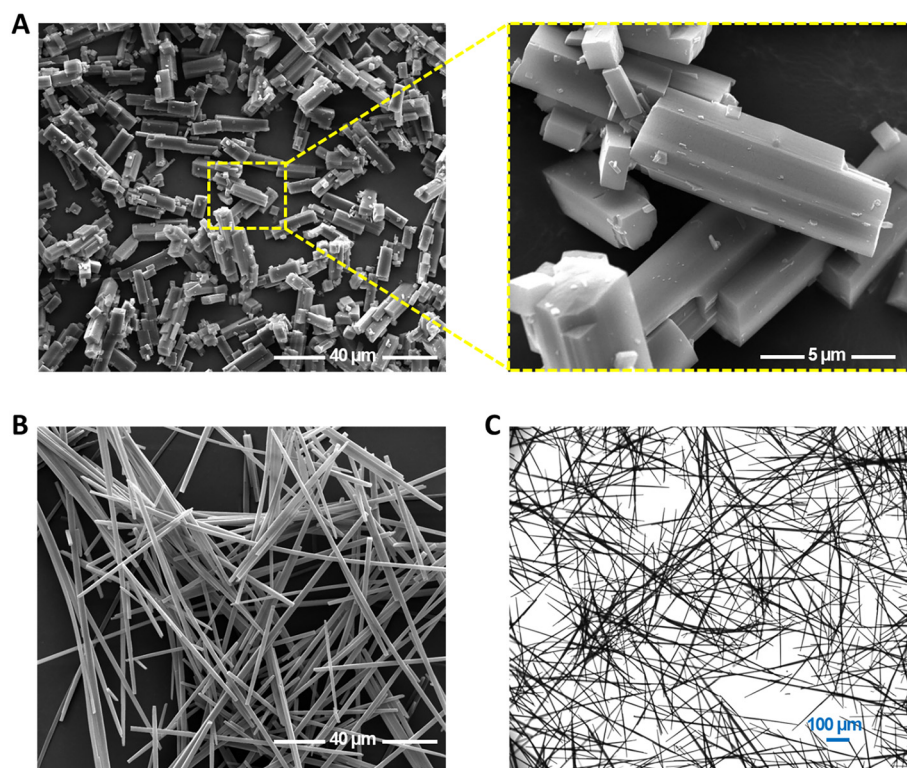

Fig. 4 (A) Scanning electron microscopy (SEM) image of the syringol–derived dehydrogenative compound synthesized under continuous stirring at 200 rpm, and (B) without stirring. (C) *In situ* optical microscopy image captured 5 min after initiating the reaction on a microscope slide.

material's hierarchical structure: the strong bonds provide molecular integrity, while the extensive network of π–π stacking and intermolecular hydrogen bonds creates a high lattice energy that must be overcome for sublimation or decomposition.

Previous studies of biomimetic polymerization of diphenoquinones and lignin-like polymers using different enzyme systems (HRP, soybean peroxidase, *Coprinus cinereus* peroxidase, and fungal/plant laccases) and various monomers are summarized in Table S2. Most of these reports concentrate on fundamental lignin biosynthesis and on the molecular-level characterization of dimeric or oligomeric products. Although HRP frequently yields high conversion and good product purity, its capacity to generate defined microscale structures, such as ordered morphologies, crystallinity, and controlled growth kinetics, has not been comprehensively examined.

In contrast, our work demonstrates that HRP-mediated coupling can provide a green and efficient approach to lignin-derived material valorization, enabling the direct formation of nano-/microrod diphenoquinone crystals without the multi-step syntheses and extensive purification. This unique combination of enzymatic, bottom-up synthesis and robust, self-assembled crystallinity opens exciting avenues for advanced materials. By using this enzymatic reaction within nanoscale or microscale templates or domains, it should be possible to direct the self-assembly process. This would enable sustainable fabrication of anisotropic, high-aspect-ratio nanostructures (*e.g.*, nanowires, nanorods) with precise dimensional control.

Cyclic voltammetry analysis

To explore the potential applications of biologically synthesized diphenoquinones and to confirm its structural identity with the chemically synthesized counterpart, we evaluated its electrochemical redox activity using a cyclic voltammetry technique, following the previous work.[21] The syringol-derived diephnoquinone was physisorbed on a carbon conductive cloth working electrode (Pt plate as a counter). The resulting stable and well-defined voltammograms confirm that the diphenoquinone can be effectively immobilized on a conductive support to create an electrochemically active interface (Fig. S5). The voltammogram exhibits a single, quasi-reversible redox activity, corresponding to a concerted two-electron, two-proton ($2e^-/2H^+$) transfer. During the cathodic scan (reduction, peak b in Fig. S5), the two quinone carbonyls are reduced to hydroquinone hydroxy groups. The reverse process occurs during the anodic scan (oxidation, peak a), where the hydroquinone is oxidized back to the quinone form.[21]

The formal potential ($E^{\circ\prime}$), estimated at the midpoint of the anodic and cathodic peaks, was found to be approximately 0.55 V *vs.* Ag/AgCl. While the peak-to-peak separation is larger than ideal due to the uncompensated resistance of low electrical conductivity of the material and the cell configuration, the potential is consistent with literature values for tetramethoxydiphenoquinones in acidic conditions.[21] This positive redox potential is a key feature of diphenoquinones, relatively more

positive than most widely used CO_2 capture quinones (*e.g.* anthraquinone), attributed to the extended π-conjugation across the two rings. It can better stabilizes the charge in both the radical-anion intermediate and the dianion.[21] The more positive redox potential would result in better stability in presence of oxygen.[52] Additionally, such relatively positive redox potential poses it as attractive candidates for use as positive electrode materials in various energy storage devices, such as redox flow batteries or organic batteries.[53–55] In this role, they could serve as a sustainable, alternative to commonly used redox-active molecules like (2,2,6,6-tetramethylpiperidin-1-yl) oxyl (TEMPO), offering comparable redox potentials with a robust structure that is readily derived from renewable biomass resources offering a promising pathway toward truly green and sustainable electrochemical energy storage.

Electrochemical CO_2 capture using syringol-derived diphenoquinone

To examine the electrochemical CO_2 capture capability of the diphenoquinone, we performed cyclic voltammetry measurement in a CO_2-saturated aqueous electrolyte using a three-electrode cell. First, a baseline CV was recorded under a fully purged N_2 atmosphere (Fig. 5A, gold-colored solid line).

Under N_2 purging and neutral conditions (0.1 M Na_2SO_4), the CV shows a two-electron redox process with two reduction features at approximately −0.28 V and −0.04 V *vs.* Ag/AgCl, and corresponding oxidation peaks around −0.20 V and +0.13 V (Fig. 5B). In the presence of CO_2, the electrochemical response changes: the distinct reduction peaks collapse into a broad catalytic wave shifted toward more positive potentials, and the oxidation transforms into a single peak near +0.20 V (Fig. 5C). This behavior is consistent with interaction between the reduced quinone species and CO_2, where binding stabilizes the reduced state, leading to positive shifts in reduction potentials.[56] The corresponding oxidation is also shifted slightly positive, as expected for oxidation of a quinone–CO_2 adduct compared to the free quinone. Cyclic voltammetry performed at different scan rates (10, 20, 30, and 50 mV s^{-1}) displayed a consistent trend (Fig. S6A–C). It should also be noted that local pH changes can also influence the observed redox potentials. In an unbuffered electrolyte, the reduced quinone may undergo protonation, which increases the local alkalinity and provides a pH-swing pathway for CO_2 capture. Such pH variations at the electrode interface can therefore contribute to the shifts in potential observed alongside quinone–CO_2 interactions.

A control experiment on a bare carbon cloth electrode (Fig. S6D) was performed to confirm the active role of the catalyst. The resulting voltammogram showed no discernible redox peaks or catalytic activity in the presence of CO_2 indicating that the carbon support is inert and that the observed electrochemical CO_2 capture originates exclusively from the immobilized syringol diphenoquinone.

Oxygen tolerance is indeed critical for electrochemical CO_2-capture systems to access the reduced quinone species that form the CO_2 adduct. Our biomimetic synthesis strategy for
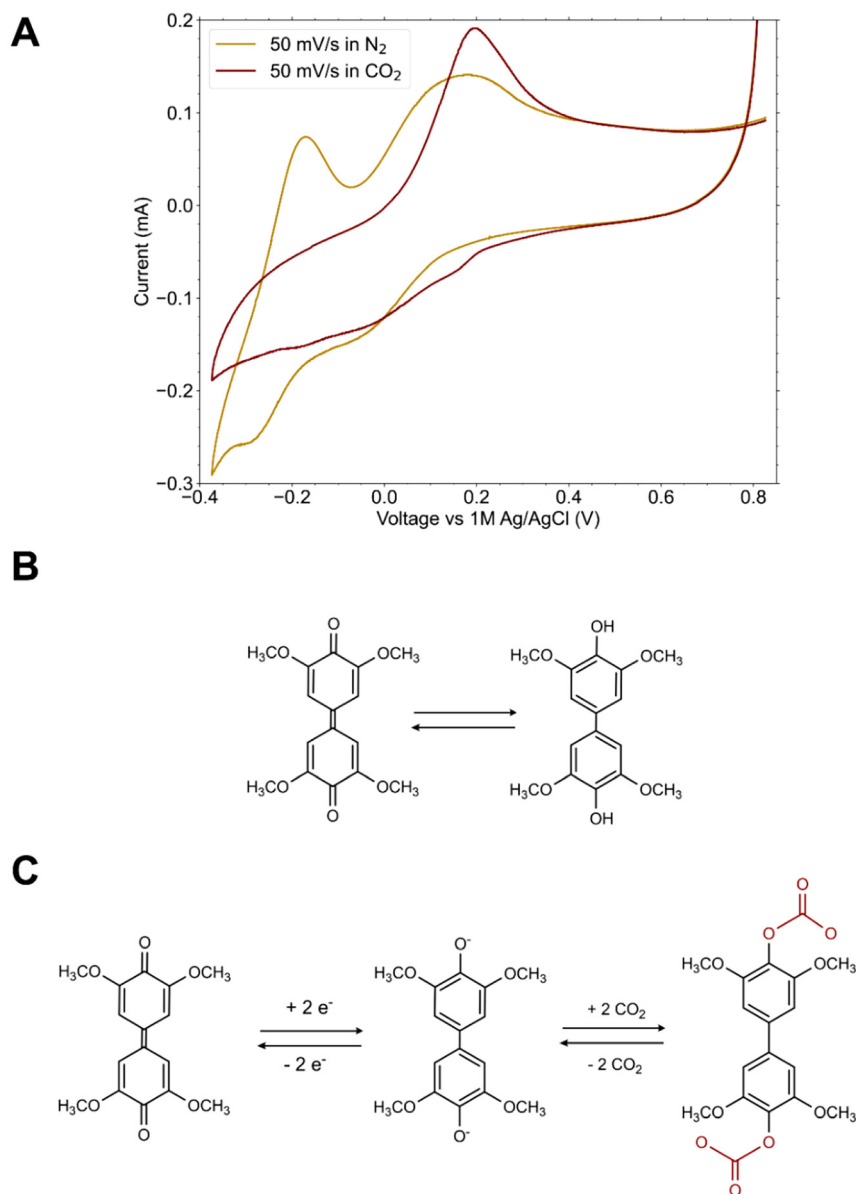
Fig. 5 Cyclic voltammogram of diphenoquinone (A) with 0.1 M Na_2SO_4 electrolyte and their intermediates with (B) N_2 and (C) CO_2 gas flow. The reaction scheme in C demonstrates the proposed nucleophilicity-swing CO_2 capture mechanism.

diphenoquinone follows the rational design rules established in previous studies for oxygen-stable quinones. The redox potential for CO_2 reduction with diphenoquinone is more positive than that reported for common quinone derivatives such as anthraquinone. Prior studies have shown that lower (more negative) redox potentials correspond to stronger CO_2 binding (greater affinity toward CO_2 complexation) but reduced oxygen stability.[16,18,53] By contrast, the relatively more positive potential of diphenoquinone may indicate improved oxygen tolerance and a weaker yet more balanced interaction with CO_2, potentially lowering the energetic cost of release while still enabling effective capture. In addition, the methoxy substituents provide steric shielding and electronic stabiliz-ation that can hinder O_2 access and suppress parasitic side

reactions, mechanisms that align with established strategies for enhancing oxygen stability in quinone-based redox systems.[18,55] This balance makes diphenoquinone a promising candidate for electrochemical carbon capture in oxygen-con-taining environments.

To translate this observed catalytic activity into a practical measure of performance, we transitioned from cyclic voltam-metry to an electrolysis H-cell system designed to quantify the material's total CO_2 capture capacity (Fig. S7 and S8). Operation in the H-cell introduces additional resistive and kinetic losses, so an overpotential of approximately ±1.0 V was required to drive the electron-transfer and CO_2-binding/release reactions at an appreciable rate. To measure, first, the working electrode was held at a constant potential of −1.0 V vs. Ag/AgCl

while CO_2 was bubbled through the electrolyte at 30 sccm. This capture step was continued until the cathodic current decayed to a steady-state value below 100 µA, ensuring sufficient time for the electrochemically reduced diphenoquinone to react with and capture CO_2. Subsequently, the system was purged with N_2 at 30 sccm, and the captured CO_2 was released by holding the electrode potential at +1.0 V vs. Ag/AgCl until the resulting anodic current decayed below 100 µA.

Fig. 6A and B show the correlated profiles of potential, current, total charge passed, and downstream CO_2 concentration during the capture and release cycles. During the capture phase at −1.0 V, the cathodic current decayed exponentially as the diphenoquinone on the electrode surface was progressively reduced and reacted with the constantly supplied CO_2. Simultaneously, we observed the solution changing to dark yellow (Fig. S8A). This color change likely indicates leaching of the reduced, charged quinone species into the electrolyte. This dissolution represents a loss of active material and is a probable cause for the measured capacity being lower than the theoretical maximum.

After the capture step, the gas flow was switched to N_2, allowing the CO_2 sensor to establish a stable baseline. During
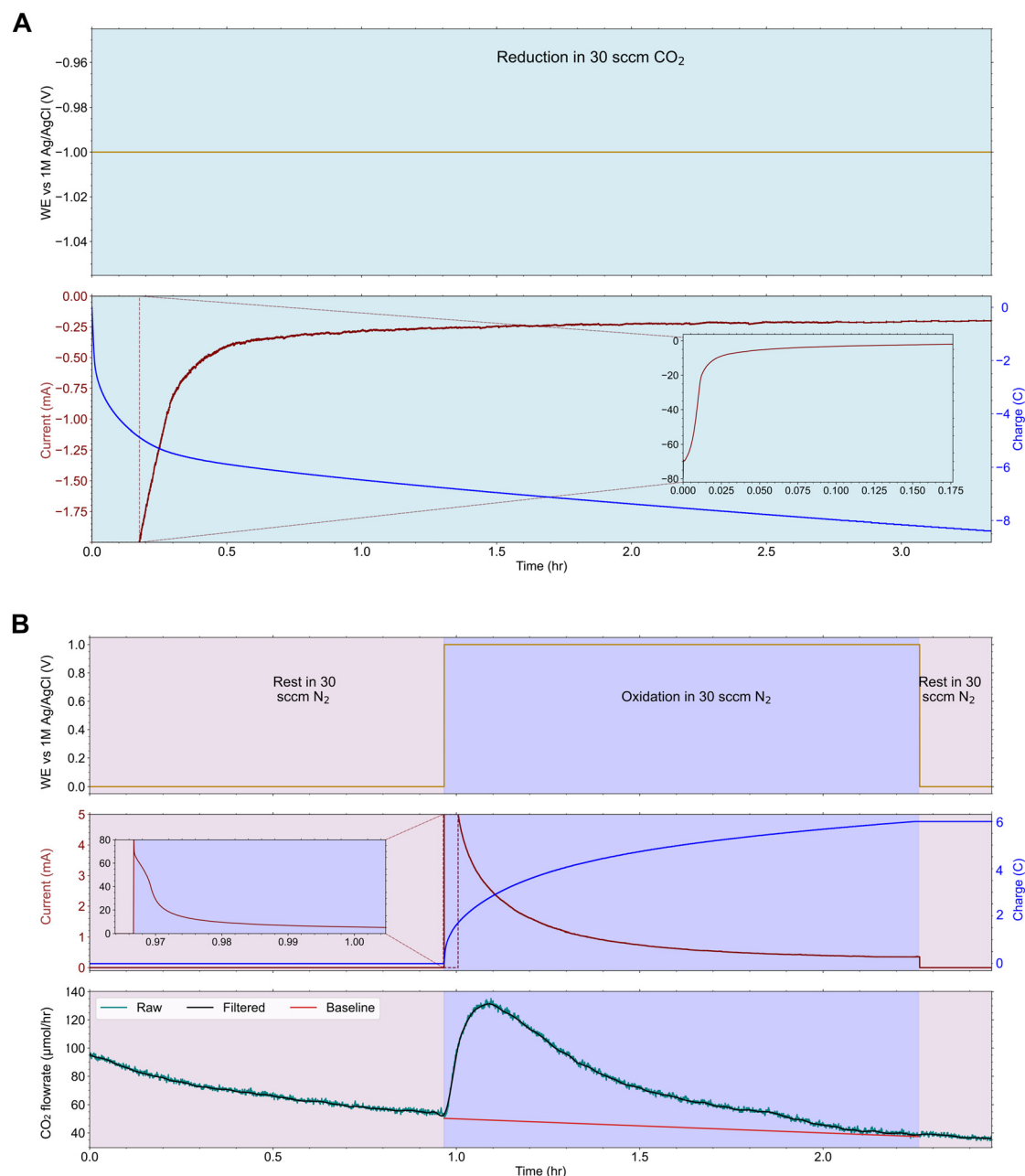

Fig. 6 Measurement of CO_2 capture capacity of the syringol diphenoquinone, profiles of voltage, current, CO_2 flow during (A) reduction for CO_2 capture and (B) release.

this N_2 purge period (rest), dissolved CO_2 in the electrolyte was gradually stripped out, causing the CO_2 flow signal to decrease until a steady baseline was reached. Upon applying an oxidative potential of +1.0 V to trigger the release, a distinct peak in the downstream CO_2 concentration was immediately observed. This provides direct, evidence that the CO_2 captured by the reduced diphenoquinone was successfully released upon oxidation. Concurrently, the solution color lightened (Fig. S8B), consistent with the oxidation of the leached species. As the anodic current decayed, the CO_2 release rate gradually returned to the baseline.

By integrating the area under this CO_2 release peak and subtracting the linear baseline, the total amount of electrochemically released CO_2 was quantified as 36.7 µmol. Based on the initial loading of 19.4 mg of diphenoquinone (theoretical capacity: 6.55 mmol CO_2 per g), this corresponds to a specific capacity of 1.9 mmol CO_2 per g. This yields a faradaic efficiency of 29% for the complete capture-and-release cycle under these initial, unoptimized conditions. The primary factor limiting the efficiency is likely the observed dissolution of the reduced active material.

To verify that the observed CO_2 capture and release originated from the coated diphenoquinone and not the electrode support, a reference experiment was conducted with a bare carbon felt electrode (Fig. S9). This control experiment proves that the rapid, potential-triggered capture and release of CO_2 is exclusively mediated by the immobilized diphenoquinone. After the experiment, upon disassembly, the separator membrane facing the working electrode was visibly stained, and the electrolyte remained colored (Fig. S10A–D), confirming our hypothesis that the electrochemically reduced hydroquinone species has some solubility, leading to active material loss. When exposed to air, the color of the stained membrane and solution intensified to a dark orange, consistent with the rapid, spontaneous oxidation of the any remaining unstable reduced species back to the stable diphenoquinone form. These observations imply that material stability and immobilization as key challenges for practical application.

Improving phase stability by minimizing solubilization of the redox-active species will be important for future CO_2-capture optimization. As shown in Fig. S10, most diphenoquinone remains in the solid phase after cycling, suggesting that only a limited amount becomes soluble under reducing conditions. Although quantification of the dissolved species was not feasible in this work, any soluble fraction is still expected to participate in the nucleophilicity-swing mechanism. For improved stability and performance, future studies will require rigorous quantification of the soluble fraction and identification of by-products using dedicated analytical methods (e.g., calibrated UV-Vis or LC/MS of the supernatant).[17] Furthermore, distinguishing the respective contributions of pH-swing and nucleophilicity-driven capture during scale-up will require advanced in situ techniques such as electrochemical fluorescence microscopy, representing an important direction for future investigation of this system.[20]

Initial electrochemical CO_2 capture studies with anthraquinones and quinonoids faced significant obstacles arising from their poor solubility, instability, and undesired dissolution or loss in the electrolyte during repetitive cycles. Dissolution of the active material led to low efficiency, capacity fading, and operational challenges. Over time, improved system performance, stability, and scalability allow quinone-based electrochemical CO_2 capture to progress from inefficient, loss-prone, homogeneous systems to robust, reusable, and higher-capacity electrode architectures.[13,18,57] This development can be implemented in our future works for practical and energy-efficient redox-active carbon capture technologies.

While the initial faradaic efficiency is modest, this work represents a critical first step in establishing biologically synthesized diphenoquinones, a class of molecules readily accessible from lignocellulosic biomass, as a new platform for electrochemical CO_2 capture. Unlike conventional amine-based systems that require significant thermal energy for regeneration, or catalysts based on scarce and toxic metals, our approach offers a pathway founded on sustainable principles: a renewable organic molecule driven by low chemical waste release and green method.

This work demonstrates the feasibility of using a lignin-derived molecular catalyst for electrochemical CO_2 capture, synthesized via a mild enzymatic route without severe chemical or thermal modification (Fig. 7). This electricity-driven approach leverages the molecule's intrinsic electronic properties, shifting the paradigm from energy-intensive thermal cycles. The catalyst shows promising initial capacity, though its long-term cyclability is currently limited by the physical instability of the reduced form, which is a limitation we
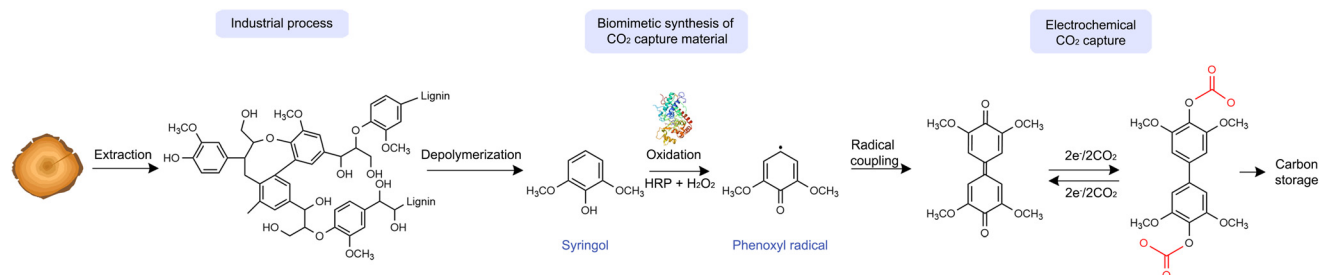

Fig. 7 Schematic illustration of an electrochemical CO_2 capture process using lignin-derived diphenoquinone.

believe is addressable through future design. Ultimately, it is believed that this study opens a new, energy-efficient pathway for lignin valorization in sustainable carbon management technologies.

Conclusion

In summary, this study demonstrates the first application of a biomass-derivable diphenoquinone for electrochemical CO_2 capture. We developed a highly selective, one-pot enzymatic synthesis that converts the lignin monomer syringol into a crystalline C4–C4′ linked diphenoquinone dimer. This biomimetic route avoids complex purification, offering a sustainable alternative to conventional syntheses. Comprehensive structural analyses confirmed the material's identity and its self-assembly into π-stacked crystalline structures. We have successfully validated this material's ability to electrochemically capture and release CO_2, achieving a specific capacity of 1.9 mmol CO_2 per g. While promising, this initial performance is primarily limited by the dissolution of the reduced active material, not by the intrinsic chemistry. This stability issue presents a clear opportunity for future improvement through molecular engineering and enhanced immobilization strategies. This work establishes a new class of renewable, redox-active molecules for carbon capture. By harnessing enzymatic synthesis to create functional materials from biomass, our approach provides a critical foundation for developing truly green technologies that contribute to a circular carbon economy.

Materials and methods

Materials

All chemical used in this work, including 2,6-dimethoxyphenol (syringol), horseradish peroxidase (HRP), 30% hydrogen peroxide solution (H_2O_2), sodium dihydrogen phosphate ($NaH_2PO_4 \cdot 2H_2O$), sodium phosphate dibasic heptahydrate ($Na_2HPO_4 \cdot 7H_2O$), sulfuric acid (H_2SO_4), sodium sulfate (Na_2SO_4), potassium chloride (KCl), sodium chloride (NaCl), polyvinylidene fluoride (PVDF), N-methylpyrrolidone (NMP), were purchased from Sigma-Aldrich and used as received. Carbon cloth, conductive carbon black (CB) and Ag/AgCl reference electrode and Pt electrode were purchased from MTI Corporation. An anion exchange membrane (DSVN, AGC Engineering), a graphite rod (Electron Microscopy Sciences), gas flow controllers (Seirra), SprintIR CO_2 sensor (CO2met) were used for electrochemical CO_2 capture and release measurement. Carbon dioxide (CO_2, purity 99.9%) and nitrogen (purity, 99.9%) were obtained from Shin Yang Gas Co. (Seoul, Korea).

Synthesis of dehydrogenation compounds

For synthesis of a dehydrogenation compound, end-wise polymerization (Zutropt) method was used. Three solutions were prepared for the synthesis of diphenoquinone. Solution A: 10 mM sodium phosphate buffer (94 mL, pH 6.5) containing 200 mg syringol and 6 mL acetone. Solution B: 10 mM sodium phosphate buffer (100 mL, pH 6.5) containing 200 μL H_2O_2 (30 wt%). Solution C: 10 mM sodium phosphate buffer (100 mL, pH 6.5) containing 20 mg HRP (150–250 units per mg solid). Solutions A and B were slowly added to the solution C with/without stirring over 2 h using peristaltic pump at room temperature in the dark. After addition of solutions A and B, the mixture was further stirred for an additional 2 h. The synthesized diphenoquinone was collected by centrifugation and washed three times with deionized water, which was lyophilized to recover solid powder (yield ~90 wt% of diphenoquinone).

Characterizations

FT-IR was conducted to analyze the chemical bonding and functional groups present in the samples using a Thermo Fisher Nicolet iS50. Nuclear magnetic resonance (NMR) spectroscopy was performed by dissolving the diphenoquinone in a deuterated form of dimethyl sulfoxide (DMSO-d_6). Spectra were collected with an Agilent DD2 600 MHz spectrometer equipped with a ONE probe. Thermogravimetric analysis (TGA) was performed using a TA Instrument SDT Q600. The temperature range for the test was from 25 to 800 °C at a heating rate of 5 °C min^{-1}. Alumina pans were used for the samples. Scanning electron microscopy (SEM) images were taken with a FE-SEM Regulus.

For liquid chromatography-tandem mass spectrometry (LC-MS/MS) analysis, a sample 3 μL was injected into Thermo vanquish HPLC system equipped with Kinetex 2.6 μm C18 column (phenomenex, 2.6 μm 100 Å, 2.1 × 100 mm). Using the mobile phase A (0.1% FA in DW) and the mobile phase B (0.1% FA in MeOH), separation was performed via following steps: 2 min of isocratic flow in 50% mobile phase B; 50% mobile phase B linear to 100% until 18 min; 10 min of isocratic flow in 100% mobile phase B; 100% mobile phase B linear to 50% for 0.01 min; 4.99 min of isocratic flow in 50% mobile phase B. The total separation was performed for 35 min, temperature of the column oven was 40 °C, and the flow rate was 0.4 mL min^{-1}.

For MS acquisitions, a Q-Exactive mass spectrometer was utilized. The capillary temperature was set at 360 °C and ion spray energy was set to 4.5 kV in positive mode. The sheath, auxiliary, and sweep gas flow rates were set to 50, 10, 0 arbitrary units, respectively. In full MS mode, mass scans were obtained at a resolution of 17 500. The automatic gain control (AGC) value was set to 1×10^5, the maximum injection time was 100 ms, and the scan range was 150–650 m/z. In Selected ion monitoring mode, the data were obtained at a resolution of 35 000. The AGC value was set to 1×10^6, the maximum injection time was 50 ms, and the isolation window was 1.0 m/z. All mass spectrometry data and spectra were analyzed using Thermo Xcalibur version 4.5 SP1.

The molecular weight distributions of the diphenoquinone were measured using a Tosoh EcoSEC HLC-8320 gel per-

meation chromatography (GPC) system equipped with RI detector. The sample was dissolved in chloroform with a concentration of 3 mg mL^{-1}. The columns used were Shodex LF-G (guard), two of Shodex LF-804 and Shodex KF-802.5. The column flow rate was 1.0 mL min^{-1} at 40 °C. The polystyrene GPC standards were used for calibration. The sample was observed using a quantitative CMOS camera (ORCA-Quest, Hamamatsu, Japan) connected to a motorized microscope (IX-73, Olympus, Japan), described in the literature.[58]

X-ray diffraction and pair distribution function

The total X-ray scattering data were collected at beamline P21.1 at DESY with an X-ray wavelength of 0.122 Å using a 4096 × 4096 px2 2D detector (PerkinElmer). Azimuthal integration and calibrations were performed using the pyFAI package. PDFs were generated with Q_{max} = 25 Å^{-1}, $Q_{max,inst}$ = 26 Å^{-1}, Q_{min} = 0.1 Å^{-1}, and r_{poly} = 0.9 using the xPDFsuite.[59] The analysis focused on the direct assignment of peaks in the experimental $G(r)$. Peak positions were correlated with known intramolecular bond lengths and expected intermolecular distances derived from literature values for similar organic compounds. The solid diphenoquinone samples were contained in epoxy-sealed glass capillaries with 0.5 mm diameter.

Electrochemical experiments

Cyclic voltammetry measurements in acidic environment were performed using a VersaSTAT 4 potentiostat (AMETEK) in a standard three-electrode configuration. Working electrodes were prepared by immersing a 1 cm × 1 cm piece of carbon cloth into a saturated acetone solution of the diphenoquinone (or quinhydrone), followed by air-drying to achieve physisorption of the active material onto the surface. A platinum wire served as the counter electrode, and a Ag/AgCl electrode (saturated with 3 M KCl) was used as the reference. All measurements in acidic environment were conducted in a 0.1 M H$_2$SO$_4$ aqueous electrolyte at a scan rate of 20 mV s^{-1} (data shown in Fig. S5).

The electrochemical response to N$_2$ and CO$_2$ was examined in a three-electrode cell configuration with an Ag/AgCl reference electrode (at 1 M KCl). The electrolyte was a 0.1 M Na$_2$SO$_4$ aqueous solution. The electrolyte was first deaerated by purging with N$_2$ for 30 minutes. Subsequently, the solution was saturated with CO$_2$ by purging for an additional 30 minutes. Cyclic voltammograms were then recorded between −0.4 V and 0.8 V vs. Ag/AgCl under a constant CO$_2$ flow at a scan rate of 10 mV s^{-1} to 50 mV s^{-1} (data shown in Fig. 5A).

Quantitative CO$_2$ capture and release experiments were performed in a two-compartment H-cell (50 mL total volume) separated by an anion exchange membrane. Each compartment was filled with 40 mL of 0.5 M NaCl electrolyte, leaving a 10 mL headspace. A graphite rod was used as the counter electrode. The working electrode was a carbon felt electrode either coated with the diphenoquinone or left bare for control experiments. Working electrode with diphenoquinone was fabricated using a 2 cm × 1 cm carbon felt support. An ink was prepared

by mixing the redox active material (diphenoquinone/quinhydrone), PVDF binder, and CB conductive additive in a mass ratio of 8 : 1 : 1 in NMP solvent, respectively. This slurry was then applied to a masked 1 cm × 1 cm area on both sides of the carbon felt using the Doctor Blade method. The coated electrodes were subsequently dried in a vacuum oven at 100 °C to remove the NMP. An Ag/AgCl electrode (in 1 M KCl) served as the reference. The experiments were conducted using a Biologic SP-300 potentiostat in chronoamperometry mode. The electrolyte was pre-saturated with CO$_2$ for 1 h before the reduction step, and CO$_2$ flow was maintained during charging to ensure a constant dissolved CO$_2$ concentration. After charging, the headspace was switched to N$_2$ for 1 h to remove dissolved CO$_2$, and the discharge step was then conducted under continuous N$_2$ flow. Gas flow to the working electrode compartment was controlled using mass flow controllers and CO$_2$ concentration in the outlet gas stream was continuously monitored using a 5% SprintIR CO$_2$ sensor, which was protected from moisture by an in-line drying tube (Drierite).

Computational analysis

All molecular structures were fully optimized using the Gaussian 16 software package, employing density functional theory (DFT) calculations with the M06-2X meta-hybrid functional and the 6-31+G(2d,2p) basis set. The computational protocol included several parameters to ensure an accurate description of the radical species: an ultrafine integration grid was implemented to provide high numerical precision for exchange–correlation functional integration; symmetry constraints were disabled to prevent bias in spin density localization; and the extended quadratic convergence algorithm was employed to achieve stable convergence for this open-shell system.

The M06-2X functional was specifically chosen due to its superior performance in describing medium-range correlation effects and its balanced treatment of both thermochemistry and kinetics for radical species, incorporating 54% Hartree–Fock exchange, which is crucial for accurate representation of unpaired electron systems. The 6-31+G(2d,2p) basis set was selected to provide a comprehensive description of both valence and diffuse orbitals, with the diffuse functions being particularly important for the proper characterization of radical anions, and the polarization functions essential for accurate geometric and electronic properties of aromatic radical systems.

Following successful geometry optimization, comprehensive spin density analysis was performed using the Multiwfn program, which calculates spin density as the difference between alpha and beta electron densities at each point in space, providing direct quantitative insight into the spatial distribution and localization of unpaired electrons throughout the molecular framework. The spin density analysis specifically focused on four chemically relevant potential radical sites within the aromatic system: the oxygen atom, two symmetry-equivalent ortho-positioned carbon atoms, and the para-positioned carbon atom, with atomic spin populations.

Author contributions

HK: conceptualization, methodology, investigation, writing – original draft preparation. OS: methodology, investigation. SU: methodology, investigation. GSA: methodology, investigation. NTT: methodology, investigation. HC: methodology, investigation. CS: methodology, investigation. SSK: methodology, investigation. BK: methodology, investigation. KJ: methodology, investigation, writing – original draft preparation. KA: methodology, investigation, writing – review & editing KHK: conceptualization, supervision, funding acquisition, writing – review & editing. All authors approved the final manuscript.

Conflicts of interest

There are no conflicts to declare.

Data availability

The supporting data has been provided as part of the supplementary information (SI). Supplementary information: LC-MS chromatogram, photo of the synthesized products, TGA, CV and Table S1 and 2. See DOI: https://doi.org/10.1039/d5gc05304h.

Acknowledgements

References

1 A. D. N. Kamkeng, M. Wang, J. Hu, W. Du and F. Qian, *Chem. Eng. J.*, 2021, **409**, 128138.

2 M. Bui, C. S. Adjiman, A. Bardow, E. J. Anthony, A. Boston, S. Brown, P. S. Fennell, S. Fuss, A. Galindo, L. A. Hackett, J. P. Hallett, H. J. Herzog, G. Jackson, J. Kemper, S. Krevor, G. C. Maitland, M. Matuszewski, I. S. Metcalfe, C. Petit, G. Puxty, J. Reimer, D. M. Reiner, E. S. Rubin, S. A. Scott, N. Shah, B. Smit, J. P. M. Trusler, P. Webley, J. Wilcox and N. Mac Dowell, *Energy Environ. Sci.*, 2018, **11**, 1062–1176.

3 W. Gao, S. Liang, R. Wang, Q. Jiang, Y. Zhang, Q. Zheng, B. Xie, C. Y. Toe, X. Zhu, J. Wang, L. Huang, Y. Gao, Z. Wang, C. Jo, Q. Wang, L. Wang, Y. Liu, B. Louis, J. Scott, A. C. Roger, R. Amal, H. He and S. E. Park, *Chem. Soc. Rev.*, 2020, **49**, 8584–8686.

4 M. Mohamadi-Baghmolaei, A. Hajizadeh, P. Zahedizadeh, R. Azin and S. Zendehboudi, *Energy*, 2021, **214**, 118715.

5 K. Veltman, B. Singh and E. G. Hertwich, *Environ. Sci. Technol.*, 2010, **44**, 1496–1502.

6 H. Kim, S. J. Hwang and K. S. Lee, *Environ. Sci. Technol.*, 2015, **49**, 1478–1485.

7 G. H. Choi, H. J. Song, S. Lee, J. Y. Kim, M.-W. Moon and P. J. Yoo, *Nano Energy*, 2023, **112**, 108512.

8 K. M. Diederichsen, R. Sharifian, J. S. Kang, Y. Liu, S. Kim, B. M. Gallant, D. Vermaas and T. A. Hatton, *Nat. Rev. Methods Primers*, 2022, **2**, 68.

9 A. M. Zito, L. E. Clarke, J. M. Barlow, D. Bím, Z. S. Zhang, K. M. Ripley, C. Li, A. Kummeth, M. E. Leonard, A. N. Alexandrova, F. R. Brushett and J. Y. Yang, *Chem. Rev.*, 2023, **123**, 8069–8098.

10 D. G. Kwabi, K. X. Lin, Y. L. Ji, E. F. Kerr, M. A. Goulet, D. De Porcellinis, D. P. Tabor, D. A. Pollack, A. Aspuru-Guzik, R. G. Gordon and M. J. Aziz, *Joule*, 2018, **2**, 1894–1906.

11 K. X. Lin, Q. Chen, M. R. Gerhardt, L. C. Tong, S. B. Kim, L. Eisenach, A. W. Valle, D. Hardee, R. G. Gordon, M. J. Aziz and M. P. Marshak, *Science*, 2015, **349**, 1529–1532.

12 M. Wu, M. Bahari, Y. Jing, K. Amini, E. M. Fell, T. Y. George, R. G. Gordon and M. J. Aziz, *Batteries Supercaps*, 2022, **5**, e202200009.

13 Y. Liu, H.-Z. Ye, K. M. Diederichsen, T. Van Voorhis and T. A. Hatton, *Nat. Commun.*, 2020, **11**, 2278.

14 B. Gurkan, F. Simeon and T. A. Hatton, *ACS Sustainable Chem. Eng.*, 2015, **3**, 1394–1405.

15 K. M. Diederichsen, Y. Y. Liu, N. Ozbek, H. Seo and T. A. Hatton, *Joule*, 2022, **6**, 221–239.

16 J. M. Barlow and J. Y. Yang, *J. Am. Chem. Soc.*, 2022, **144**, 14161–14169.

17 D. Wielend, D. H. Apaydin and N. S. Sariciftci, *J. Mater. Chem. A*, 2018, **6**, 15095–15101.

18 Y. Jing, K. Amini, D. Xi, S. Jin, A. M. Alfaraidi, E. F. Kerr, R. G. Gordon and M. J. Aziz, *ACS Energy Lett.*, 2024, **9**, 3526–3535.

19 C. Huang, C. Liu, K. Wu, H. Yue, S. Tang, H. Lu and B. Liang, *Energy Fuels*, 2019, **33**, 3380–3389.

20 K. Amini, T. Cochard, Y. Jing, J. D. Sosa, D. Xi, M. Alberts, M. S. Emanuel, E. F. Kerr, R. G. Gordon and M. J. Aziz, *Nat. Chem. Eng.*, 2024, **1**, 774–786.

21 S. Néron, M. Morency, L. Chen, T. Maris, D. Rochefort, R. Iftimie and J. D. Wuest, *J. Org. Chem.*, 2022, **87**, 7673–7695.

22 G. S. Baviera and P. M. Donate, *Beilstein J. Org. Chem.*, 2021, **17**, 2028–2050.

23 A. Beaucamp, M. Muddasar, I. S. Amiinu, M. M. Leite, M. Culebras, K. Latha, M. C. Gutiérrez, D. Rodriguez-Padron, F. del Monte, T. Kennedy, K. M. Ryan, R. Luque, M. M. Titirici and M. N. Collins, *Green Chem.*, 2022, **24**, 8193–8226.

24 K. H. Kim, T. Dutta, E. D. Walter, N. G. Isern, J. R. Cort, B. A. Simmons and S. Singh, *ACS Sustainable Chem. Eng.*, 2017, **5**, 3913–3919.

25 B. Zhao, M. Borghei, T. Zou, L. Wang, L.-S. Johansson, J. Majoinen, M. H. Sipponen, M. österberg, B. D. Mattos and O. J. Rojas, *ACS Nano*, 2021, **15**, 6774–6786.

26 D. Barker-Rothschild, J. Chen, Z. Wan, S. Renneckar, I. Burgert, Y. Ding, Y. Lu and O. J. Rojas, *Chem. Soc. Rev.*, 2025, **54**, 623–652.

27 Y. Cui, B. He, Y. Lei, Y. Liang, W. Zhao, J. Sun and X. Liu, *Chin. J. Chem. Eng.*, 2023, **54**, 89–97.

28 A. Ghorai and H. Chung, *Adv. Mater.*, 2024, **36**, 2406610.

29 A. Ghorai and H. Chung, *Adv. Funct. Mater.*, 2024, **34**, 2403035.

30 A. E. Harman-Ware, R. M. Happs, B. H. Davison and M. F. Davis, *Biotechnol. Biofuels*, 2017, **10**, 281.

31 T. Kishimoto, N. Takahashi, M. Hamada and N. Nakajima, *J. Agric. Food Chem.*, 2015, **63**, 2277–2283.

32 B. Saake, D. S. Argyropoulos, O. Beinhoff and O. Faix, *Phytochemistry*, 1996, **43**, 499–507.

33 Á. Sánchez-González, F. J. Martín-Martínez and J. Dobado, *J. Mol. Model.*, 2017, **23**, 1–10.

34 W. R. Russell, A. R. Forrester, A. Chesson and M. J. Burkitt, *Arch. Biochem. Biophys.*, 1996, **332**, 357–366.

35 K. Morreel, O. Dima, H. Kim, F. Lu, C. Niculaes, R. Vanholme, R. Dauwe, G. Goeminne, D. Inzé and E. Messens, *Plant Physiol.*, 2010, **153**, 1464–1478.

36 N. Giummarella, I. V. Pylypchuk, O. Sevastyanova and M. Lawoko, *ACS Sustainable Chem. Eng.*, 2020, **8**, 10983–10994.

37 C. Crestini, H. Lange, M. Sette and D. S. Argyropoulos, *Green Chem.*, 2017, **19**, 4104–4121.

38 M. Dolz, D. T. Monterrey, A. Beltrán-Nogal, A. Menés-Rubio, M. Keser, D. González-Pérez, P. G. de Santos, J. Viña-González and M. Alcalde, *Methods Enzymol.*, 2023, **693**, 73–109.

39 S. Sasaki, T. Nishida, Y. Tsutsumi and R. Kondo, *FEBS Lett.*, 2004, **562**, 197–201.

40 B. Cathala and B. Monties, *Int. J. Biol. Macromol.*, 2001, **29**, 45–51.

41 H. Hwang, S.-J. Moon, K. Won, Y. H. Kim and J. W. Choi, *J. Ind. Eng. Chem.*, 2015, **26**, 390–395.

42 S.-J. Moon, M. Kwon, D. Choi, K. Won, Y. H. Kim, I.-G. Choi and J. W. Choi, *Phytochemistry*, 2012, **82**, 15–21.

43 S. Wong, W. Sytnyk and J. Wan, *Can. J. Chem.*, 1972, **50**, 3052–3057.

44 A. E. Alegría, M. López and N. Guevara, *J. Chem. Soc., Faraday Trans.*, 1996, **92**, 4965–4968.

45 H. Q. Le, M. Rusek and A. Katrusiak, *J. Phys. Chem. C*, 2023, **127**, 4310–4318.

46 Infrared Spectrum of 3,3′,5,5′-tetramethoxy-4,4′-diphenoquinone, NIST Chemistry WebBook, https://webbook.nist.gov/cgi/inchi?ID=C493743&Mask=80.

47 O. E. Adelakun, T. Kudanga, I. R. Green, M. le Roes-Hill and S. G. Burton, *Process Biochem.*, 2012, **47**, 1926–1932.

48 M. W. Terban and S. J. Billinge, *Chem. Rev.*, 2021, **122**, 1208–1272.

49 V. García-Negrón, D. G. Kizzire, O. Rios, D. J. Keffer and D. P. Harper, *Carbon*, 2020, **161**, 856–869.

50 R. Parthasarathi, R. A. Romero, A. Redondo and S. Gnanakaran, *J. Phys. Chem. Lett.*, 2011, **2**, 2660–2666.

51 Y. Zhang, F. Huo, Y. Wang, Y. Xia, X. Tan, S. Zhang and H. He, *Front. Chem.*, 2019, **7**, 78.

52 A. T. Bui, N. A. Hartley, A. J. W. Thom and A. C. Forse, *J. Phys. Chem. C*, 2022, **126**, 14163–14172.

53 W. Liu, Z. Zhao, T. Li, S. Li, H. Zhang and X. Li, *Sci. Bull.*, 2021, **66**, 457–463.

54 J. Luo, B. Hu, M. Hu, Y. Zhao and T. L. Liu, *ACS Energy Lett.*, 2019, **4**, 2220–2240.

55 Z. Zhao, C. Zhang and X. Li, *J. Energy Chem.*, 2022, **67**, 621–639.

56 F. Simeon, M. C. Stern, K. M. Diederichsen, Y. Liu, H. J. Herzog and T. A. Hatton, *J. Phys. Chem. C*, 2022, **126**, 1389–1399.

57 N. A. Hartley, S. M. Pugh, Z. Xu, D. C. Leong, A. Jaffe and A. C. Forse, *J. Mater. Chem. A*, 2023, **11**, 16221–16232.

58 K. Kim, S. Oh, B. L. Suh, J. Bae, M. Namkoong, Y. Kim, J. Yoon, H. Kim, S. Lim, I. S. Kim, I. G. Lee, M. W. Moon, K. Hur, W. Park and H. Cho, *Adv. Mater.*, 2025, **37**, 2404092.

59 X. Yang, P. Juhas, C. L. Farrow and S. J. L. Billinge, *arXiv*, 2014, arXiv:1402.3163, DOI: 10.48550/arXiv.1402.3163.